

Improvement of deconvolution–convolution treatment of axial-divergence aberration in Bragg–Brentano geometry

Takashi Ida,^{1,a)} Shoki Ono,¹ Daiki Hattan,¹ Takehiro Yoshida,¹ Yoshinobu Takatsu,¹ and Katsuhiko Nomura²

¹Advanced Ceramics Research Center, Nagoya Institute of Technology, Asahigaoka, Tajimi, Gifu 507-0071, Japan

²Inorganic Functional Materials Research Institute, National Institute of Advanced Industrial Science and Technology, Anagahora, Shimoshidami, Moriyama, Nagoya, Aichi 463-8560, Japan

(Received 5 January 2018; accepted 18 February 2018)

An improved method to correct observed shift and asymmetric deformation of diffraction peak profile caused by the axial-divergence aberration in Bragg–Brentano geometry is proposed. The method is based on deconvolution–convolution treatment applying scale transform of abscissa, Fourier transform, and cumulant analysis of an analytical model for the axial-divergence aberration. The method has been applied to the powder diffraction data of a standard LaB₆ powder (NIST SRM660a) sample, collected with a one-dimensional Si strip detector. The locations, widths and shape of the peaks in the deconvolved–convolved powder diffraction data have been analyzed. The finally obtained whole powder diffraction pattern ranging from 10° to 145° in diffraction angle has been simulated by the Pawley method applying a symmetric Pearson VII peak profile model to each peak with ten background, two peak-shift, three line-width, and two peak-shape parameters, and the R_p value of the best fit has been estimated at 4.4%. © 2018 International Centre for Diffraction Data.

[doi:10.1017/S0885715618000349]

Key words: axial-divergence aberration, Bragg–Brentano geometry, deconvolution, convolution

I. INTRODUCTION

We have previously proposed a whole-pattern deconvolution method for laboratory powder X-ray diffraction data (Ida and Toraya, 2002). It may appear to be equivalent to a curve-fitting method with a peak profile model synthesized by multiple convolutions with instrumental functions, often referred as “fundamental-parameters approach” (FPA) (Cheary and Coelho, 1992).

In theoretical and practical points of view, there are both favorable and unfavorable features in the deconvolution method. Since all the deconvolution treatment can be completed by application of the fast Fourier transform (FFT) algorithm, the computation time needed for deconvolution–convolution treatment is quite short. There is practically no restriction about the complexity about the spectroscopic profile model for the source X-ray to be assumed, as demonstrated in another article (Ida *et al.*, 2018). Deconvolution method can remove the deformation of peak profile caused by instrumental aberrations, and it will be helpful to find possible intrinsic asymmetry of diffraction peak profile, which may be caused by inhomogeneous strain, stacking fault, chemical inhomogeneity, etc. without any structure model or identification of phases.

The effects of spectroscopic profile and instrumental aberrations on the observed diffraction profile are not exactly expressed by the convolution with instrumental functions on the scale of diffraction angle 2θ , while the effect of the

spectroscopic profile of source X-ray is exactly expressed by convolution on the scale of $\ln \sin \theta$, for example. Application of appropriate scale transform can easily be implemented in the whole-pattern deconvolution–convolution method, while it is quite difficult to treat the 2θ -dependence of the instrumental function properly in the FPA method. The FPA method usually applies the instrumental function determined at the peak position to whole the diffraction peak profile, even if the tails of lower- and higher-angle sides of the peak should be affected by different instrumental functions when the observed peak is broad.

On the other hand, there is theoretical difficulty about the estimation of error propagation in the whole-pattern deconvolution–convolution method. Even if the statistical errors in the observed diffraction intensity data can be assumed to be statistically independent, the deconvolved–convolved data will lose the independence.

There was another problem in the method described in our previous report (Ida and Toraya, 2002), where the effects of axial-divergence aberration were modeled by the convolution of two component functions defined on the transformed scale of abscissa, $\chi'_- = -\ln \cos \theta$ and $\chi'_+ = \ln \sin \theta$ for the diffraction angle 2θ .

The model could simulate primary dependence of the axial-divergence aberration upon the diffraction angle, where the broadenings of the lower- and higher-angle components are proportional to $\cot \theta$ and $\tan \theta$, respectively. However, detailed cumulant analysis on the theoretical formula of axial-divergence aberration function suggests that there is a small discrepancy between the precise formula for the axial-divergence aberration and the convolution model

^{a)} Author to whom correspondence should be addressed. Electronic mail: ida.takashi@nitech.ac.jp

applied in the previous whole-pattern deconvolution treatment. In this study, the mathematical formula for the convolution model for axial-divergence aberration has been modified to meet the requirements that the lower-order cumulants of the approximate formula should have the same values as the precise formula.

II. THEORETICAL

A. Characteristics of the axial-divergence aberration function

The axial-divergence aberration function $\omega_A(\Delta 2\theta)$ for a powder diffractometer with Bragg–Brentano geometry is well approximated by the following integral formula (Ida, 1998):

$$\omega_A(\Delta 2\theta) = \frac{1}{\Psi^2} \int_{-\Psi}^{\Psi} \int_{-\Psi}^{\Psi} \left(1 - \frac{|\alpha|}{\Psi}\right) \left(1 - \frac{|\beta|}{\Psi}\right) \times \delta\left(\Delta 2\theta + \frac{(\alpha - \beta)^2}{4 \tan \theta} - \frac{(\alpha + \beta)^2 \tan \theta}{4}\right) d\alpha d\beta, \quad (1)$$

where Ψ is the axial-divergence angle defined by the ratio of the interval to the length of the Soller slits, 2θ is the diffraction angle, and $\delta(x)$ is the Dirac delta function. The characteristics of the axial-divergence aberration function $\omega_A(\Delta 2\theta)$ can be derived without solving Eq. (1) (see Appendix A).

The average position $2\theta_A$ of the function $\omega_A(2\theta)$ is given by

$$2\theta_A \equiv \int_{-\infty}^{\infty} x \omega_A(x) dx = \frac{\Psi^2}{12} (\tan \theta - \cot \theta), \quad (2)$$

and the variance $(\Delta 2\theta)_A^2$, which can be connected with the peak width, is given by

$$(\Delta 2\theta)_A^2 = \frac{17\Psi^4}{1440} \left(\tan^2 \theta + \frac{6}{17} + \cot^2 \theta \right). \quad (3)$$

The third-order central moment $(\Delta 2\theta)_A^3$, which can be connected with the asymmetry in peak shape, is given by

$$(\Delta 2\theta)_A^3 = \frac{169\Psi^6}{60480} \left(\tan^3 \theta + \frac{81 \tan \theta}{169} - \frac{81 \cot \theta}{169} - \cot^3 \theta \right), \quad (4)$$

The average, variance, and third-order central moment are identical to the first, second, and third-order cumulants of the function $\omega_A(\Delta 2\theta)$, respectively. Note that the formula previously proposed (Ida and Toraya, 2002) could only model the third-order central moment proportional to $(\tan^3 \theta - \cot^3 \theta)$.

Since the cumulant of the convolution is generally equal to the sum of cumulants of component functions, it should not be very difficult to construct an approximate convolution formula that can reproduce exact values of both the first and third-order cumulants of the function $\omega_A(2\theta)$.

It is assumed that there is no need to change the effects of the even-order cumulants of the instrumental function on the deconvolution–convolution treatment.

B. Scale transform of convolution model for axial-divergence aberration

We have noticed that slight modification of the formula for the scale transform allows us to achieve coincidence of both the first and third-order cumulants of the axial-divergence aberration function with the convolution of two asymmetric functions defined on two different scales of abscissa.

The formulas of two abscissa scales, χ_+ and χ_- , which should be used on the deconvolution–convolution treatment instead of the diffraction angle 2θ , are given by the following equation:

$$\chi_{\pm} = \pm \frac{\ln[1 + \beta \mp (1 - \beta) \cos 2\theta]}{1 - \beta}, \quad (5)$$

where β is a constant given by

$$\beta = \frac{71 - 14\sqrt{22}}{27} = 0.197562. \quad (6)$$

The derivation of the above formulas and the constant value of β in Eq. (6) is described in Appendix B.

C. Model component functions

A model for the component functions examined in this study is an extension of that used in our previous study (Ida and Toraya, 2002), modified to reproduce the shift (first-order cumulant) and asymmetric shape (third-order cumulant) of the axial-divergence aberration function. The formula for the component functions $w_{\pm}(\chi_{\pm})$ defined on the scales of χ_{\pm} is given by

$$w_{\pm}(\chi_{\pm}) = w(\pm \chi_{\pm}), \quad (7)$$

$$w(\chi) = \begin{cases} \frac{1}{\Gamma(\alpha)\gamma} \left(\frac{\chi - \delta}{\gamma}\right)^{\alpha-1} \exp\left(-\frac{\chi - \delta}{\gamma}\right) & [\delta < \chi] \\ 0 & [\chi \leq \delta], \end{cases} \quad (8)$$

where δ and γ are given by

$$\delta = \frac{\Psi^2}{12(1 - \beta)} - \alpha\gamma, \quad (9)$$

$$\gamma = \left[\frac{169}{120960\alpha(1 - \beta^3)} \right]^{1/3} \Psi^2. \quad (10)$$

The function $\Gamma(\alpha)$ in Eq. (8) is the gamma function defined by

$$\Gamma(\alpha) \equiv \int_0^{\infty} t^{\alpha-1} e^{-t} dt. \quad (11)$$

The details about the derivation of the above formulas are described in Appendix C.

The analytical formula of the Fourier transform of the function $w(\chi)$ is given by

$$W(\xi) \equiv \int_{-\infty}^{\infty} w(\chi) e^{2\pi i \xi \chi} d\chi = \frac{e^{2\pi i \xi \delta}}{(1 - 2\pi i \xi \gamma)^\alpha}. \quad (12)$$

The first- and third-order cumulants of the convolution of the component functions on 2θ -scale are then both coincided with those of the axial-divergence aberration function described in Section II.A. The second-order cumulant of the convolution model given by

$$(\Delta 2\theta)^2 = \alpha \gamma^2 (1 + \beta^2) \left(\tan^2 \theta + \frac{54}{71} + \cot^2 \theta \right) \quad (13)$$

is different from that given in Eq. (3), but the difference does not matter in the treatment applied in the method proposed in this paper, as will be shown in Section II.D.

D. Deconvolution–convolution treatment of axial-divergence aberration

Deconvolution–convolution treatment of axial-divergence aberration is divided into two steps, treatments on two abscissa scales, χ_+ and χ_- , given in Eq. (5).

When the observed powder diffraction intensity data are given as a set of diffraction angles and intensities (2θ , I), the abscissa and ordinate values are changed to (χ_\pm, η_\pm) , where the transformation of the intensity values are given by

$$\eta_+ = IC(2\theta)(\tan \theta + \beta \cot \theta), \quad (14)$$

$$\eta_- = IC(2\theta)(\cot \theta + \beta \tan \theta). \quad (15)$$

The function $C(2\theta)$ in Eqs. (14) and (15) is the geometric correction factor given by

$$C(2\theta) = \frac{2 \sin \theta \sin 2\theta}{1 + \cos^2 2\theta} \quad (16)$$

for a Bragg–Brentano powder diffractometer without a diffractive optical element.

The deconvolution–convolution process about intensities, $(\eta_\pm)_j \rightarrow (\eta'_\pm)_j$, applied here is expressed by

$$(\eta'_\pm)_j = \frac{1}{n} \sum_{k=-n/2}^{n/2} \frac{|W_\pm(\xi_k)|}{W_\pm(\xi_k)} I_k \exp\left(-\frac{2\pi i k j}{n}\right), \quad (17)$$

$$\xi_k = \frac{k}{n \Delta \chi_\pm}, \quad (18)$$

$$I_k = \sum_{j=0}^{n-1} (\eta_\pm)_j \exp\left(\frac{2\pi i k j}{n}\right), \quad (19)$$

where $\Delta \chi_\pm$ is the sampling interval on the χ_\pm scale. Multiplication by $|W_\pm(\xi_k)|$ on division by $W_\pm(\xi_k)$ in Eq. (17) confirms that the effects of even-order cumulants of the instrumental function are unchanged by the treatment (see Appendix D), even if the used model function does not precisely reproduce the even-order cumulants of the instrumental function. This treatment is equivalent to the convolution of a symmetrized instrumental function on deconvolution with an asymmetric instrumental function.

We have already suggested that this treatment can effectively smoothen the deconvolved intensity profile (Ida and Hibino, 2006), but it is rather essential to the current method, because the second-order cumulants of the convolution of the model functions are clearly different from that of the exact instrumental function, as shown in Eqs. (3) and (13). Note that the line-broadening effect of the axial divergence aberration still remains in the deconvolved–convolved data, and the effect should be modeled by the formula given in Eq. (3), if necessary.

E. Error propagation in deconvolution–convolution process

Even if the statistical errors in the observed intensity data can be assumed to be mutually independent, the errors in the deconvolved data will lose the independence on the deconvolution process. In other words, the error (covariance) matrix of the deconvolved data should have non-zero off-diagonal elements. In our previous report (Ida and Toraya, 2002), we have suggested two types of simplification to evaluate the errors in deconvolved data: (i) neglect of the off-diagonal elements of the covariance matrix and (ii) neglect of the off-diagonal elements of the weight matrix, which is identical to the inverse matrix of the covariance matrix.

The analytical results based on the former simplification assuming counting statistical errors have shown an overestimation of errors in low-intensity reflections, and those based on the latter simplification have shown an underestimation of errors in high-intensity reflections (Ida and Toraya, 2002). As it is currently well known that powder diffraction data are also affected by other types of statistical errors (Ida *et al.*, 2009), we can apply the latter simplification as the more appropriate treatment of the errors in the deconvolved data almost in no doubt.

The statistical variance in the deconvolved data are then evaluated as the reciprocal of the correlation of the reciprocal of the source variance with the squared instrumental function (Ida and Toraya, 2002). The treatment may appear to refuse zero-count data, but a Bayesian interpretation (see Appendix E) or use of calculated intensity instead of the observed count (Antoniadis *et al.*, 1990) will solve the problem.

III. ANALYSIS OF EXPERIMENTAL DATA

A. Experimental

Powder diffraction data of standard LaB₆ powder (NIST SRM660a) were collected with a powder diffraction measurement system (PANalytical, X'Pert PRO MTD) of θ – θ -type goniometer equipped with a micro-focus Cu-target sealed tube with the effective focal width of $W_S = 0.04$ mm operated at 45 kV and 40 mA, and a one-dimensional Si strip detector (PANalytical X'Celerator) at the distance of $R = 240$ mm from the rotation axis of the goniometer. The interval of the detector strips was $W_D = 0.075$ mm. The 2θ -margins of the X-ray source $\Delta 2\theta_S$ and the detector $\Delta 2\theta_D$ are estimated at

$$\Delta 2\theta_S = \frac{180^\circ}{\pi} \frac{0.04}{240} = 0.0095^\circ, \quad (20)$$

$$\Delta 2\theta_D = \frac{180^\circ}{\pi} \frac{0.075}{240} = 0.0179^\circ, \quad (21)$$

and the standard statistical error in the diffraction angle, $\Delta 2\theta$, is then estimated at

$$\Delta 2\theta = \sqrt{\frac{(\Delta 2\Theta_S)^2 + (\Delta 2\Theta_D)^2}{12}} = 0.0059^\circ, \quad (22)$$

on the assumption of uniform probability distribution about the detection of X-ray photons.

Fixed-angle divergence slit of 0.5° and a couple of Soller slits with the open angle of 0.04 rad were used. Ni foil of 0.02 mm in thickness was used as a $K\beta$ filter. The one-dimensional powder diffraction intensity data were created by an automatic measurement/data-processing program (PANalytical, Data Collector) from the integration of five iterations of continuous scans for the diffraction angles ranging from 10° to 145° with the nominal step interval of 0.0167° and nominal measurement time of 10.16 s step^{-1} . Further details about the experimental conditions are described elsewhere (Ida *et al.*, submitted).

B. Optimization of the component functions

The optimum values of the shape parameter α in the model component functions were searched by fitting the Pearson VII peak profile function with the linear background to the deconvolved intensities around observed LaB_6 100-reflection. The Pearson VII function with the integral breadth of B is given by

$$f_{P7}(k; B, \mu) = \frac{1}{B} \left\{ 1 + \pi \left[\frac{\Gamma(\mu - 1/2)k}{\Gamma(\mu)B} \right]^2 \right\}^{-\mu}, \quad (23)$$

where μ is a shape parameter. The Pearson VII function becomes identical to the Gaussian function for the limit $\mu \rightarrow \infty$, modified Lorentzian, intermediate Lorentzian, and Lorentzian for $\mu = 2, 1.5,$ and 1 , respectively, and the profile will become “super-Lorentzian” for $0.5 < \mu < 1$ (Ida, 2008). The values of χ^2 of the fitting, defined by

$$\chi^2 = \sum_{j=0}^{n-1} \frac{1}{\sigma_j^2} [y_j - f(x_j)]^2, \quad (24)$$

have been evaluated for $\alpha = 0.02, 0.04, \dots, 0.98$, where $\{y_j\}$ is the deconvolved data, $f(x_j)$ is the value of the Pearson VII function, and $\{\sigma_j\}$ is the estimated error in the deconvolved data,

initially assumed to be the propagation of the counting statistical error and the 2θ -error propagation to intensity in the source data (Ida, 2016). The reason why the 2θ -error propagation is taken into account in the current analysis is explained in Appendix F.

The effects of the spectroscopic intensity distribution of the source X-ray have been removed by the deconvolution–convolution method described in another article (Ida *et al.*, 2018). The asymmetric deformation and peak-shift caused by the flat-specimen and sample-transparency aberrations have also been removed by the method previously proposed (Ida and Toraya, 2002).

Figure 1 shows the dependence of minimum χ^2 on the variation of α , where the axial-divergence angle is assumed to be $\Psi = 2.29^\circ$ (0.04 rad). The value of χ^2 has a minimum about 141 at $\alpha = 0.80$. The number of analyzed data points was $N = 63$ for the 100-reflection, and the number of adjusted parameters were $P = 6$. The larger value of χ^2 than $(N - P)$ may be caused by the difference of the intrinsic peak profile from Pearson VII function or underestimation of statistical errors.

The results of Pearson VII curve fitting to the deconvolved–convolved LaB_6 100-peak profile are shown in Figure 2(c) and (d). The shape parameter of the Pearson VII function is optimized to be $\mu = 1.00(14)$, which indicates that the profile of the deconvolved–convolved data are close to the Lorentzian profile.

The residuals of the Pearson VII fitting for the deconvolved–convolved 100-reflection shows six-node profile (six crossing points to the zero line) as can be seen in Figure 2 (d), which confirms that the intensity, peak location, width, asymmetry, and sharpness of the peak profile are reproduced by the optimized Pearson VII function. Since the apparently larger deviation from the assumed error is almost systematic, it does not mean the underestimation of errors, but rather indicates the mismatch of the Pearson VII fitting. If the systematic part of the deviation can be removed, the residuals (statistical errors) might be close to or even smaller than the assumed errors. It is concluded that there is no evidence that indicates overestimation or underestimation of errors, even though the error estimation applied here might be quite different from a traditional way.

It is also likely that the deviation is partly affected by the particle statistics (Ida and Izumi, 2011, 2013). The estimation of unknown errors should be based on a maximum-likelihood approach, but we here apply a simplified method just to avoid possible underestimation of errors in optimized profile

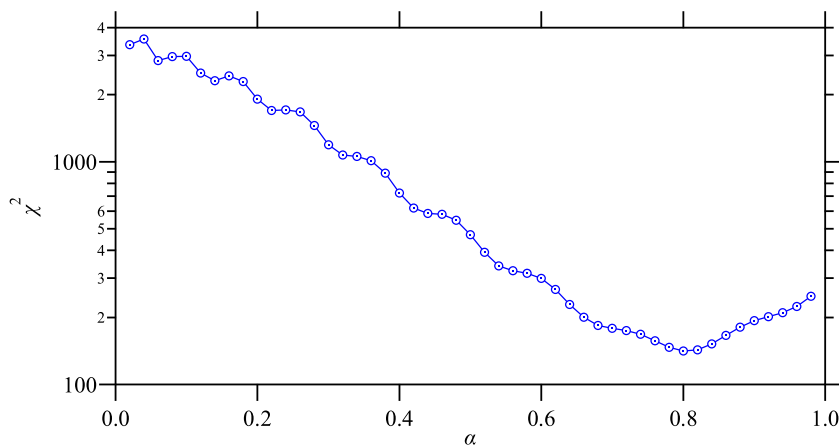


Figure 1. (Colour online) The values of χ^2 evaluated for Pearson VII fitting to the deconvolved 100-peak profile on variation of the parameter α .

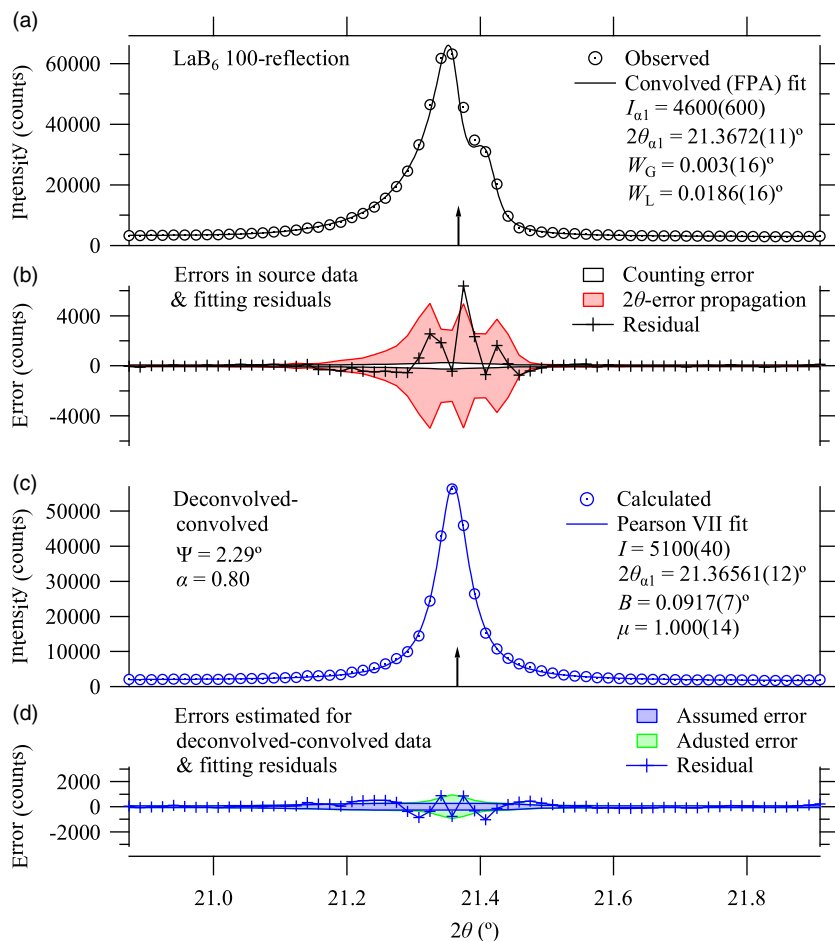


Figure 2. (Colour online) (a) Observed LaB₆ 100-reflection data and an FPA fitting curve calculated by a combination of pseudo-Voigt functions (Thompson *et al.*, 1987) with a fixed Lorentzian components (Deutsch *et al.*, 2004), and multiply convolved with the instrumental aberration functions (Ida and Kimura, 1999a; b), (b) estimated errors and fitting residuals in (a), (c) deconvolved-convolved data and the optimized symmetric Pearson VII function, and (d) estimated errors and fitting residuals in (c). Vertical arrows in (a) and (c) indicate the peak locations estimated by the FPA analysis and deconvolution-convolution treatment.

parameters. The method is based on least-squares minimization to the squared residuals $\{r_j^2\}$ by the sum of statistical variance assuming the following formula:

$$r_j^2 \approx \sigma_j^2 + f(y_{\text{obs}})_j^2, \quad (25)$$

where f is an adjustable parameter, σ_j is the initially estimated error, and $(y_{\text{obs}})_j$ is the observed intensity. The second term on the right-hand side of Eq. (25) can approximately be corresponded to the effects of particle statistics. The error values adjusted by Eq. (25) are also shown in Figure 2(d). The results of the final Pearson VII fitting shown in Figures 2(c) and 2(d) are based on the errors adjusted by the above method, but no significant difference from the results based on the initially assumed errors has been detected. The assumed errors might be overestimated, but the effect of particle statistics should be less significant on the scan with one-dimensional detector, because the integration of the intensities from the different detector strips should enhance the probability that a randomly oriented crystallite satisfies the diffraction condition, and increase the number of diffracting crystallites that contributes to the observed diffraction intensities.

C. Comparison with convolved (FPA) profile fitting to observed data

The observed diffraction data are analyzed by individual profile fitting with an FPA model, which is a diffraction peak profile model synthesized by combination of the

pseudo-Voigt function (Thompson *et al.*, 1987), CuK α emission profile (Deutsch *et al.*, 2004), and approximate instrumental aberration functions (Ida and Kimura, 1999a; b). All instrumental parameters including 11 independent parameters to determine four Lorentzian components of the normalized CuK α emission profile, axial divergence angle Ψ , equatorial divergence angle Φ , penetration depth μ^{-1} , and goniometer radius R were treated as fixed constants. The formula used for the fitting is given by the following equations:

$$f(2\theta) = b_0 + b_1(2\theta - 2\theta_1) + If_{S*A*F*T}(2\theta - 2\theta_1), \quad (26)$$

$$f_{S*A*F*T}(\Delta 2\theta) = f_S(\Delta 2\theta) * \omega_A(\Delta 2\theta) * \omega_F(\Delta 2\theta) * \omega_T(\Delta 2\theta), \quad (27)$$

$$f_S(\Delta 2\theta) = f_{TCH}(\Delta 2\theta; W_G, W_L) * f_\alpha(\Delta 2\theta), \quad (28)$$

where b_0 and b_1 are background parameters, $2\theta_1$ is the nominal $K\alpha_1$ peak position, I is the integrated intensity, and the function $f_{S*A*F*T}(2\theta)$ is the multiple convolution of the function $f_S(\Delta 2\theta)$ with the approximate instrumental aberration functions for axial-divergence $\omega_A(\Delta 2\theta)$ (Ida, 1998), flat-specimen $\omega_F(\Delta 2\theta)$ (Ida and Kimura, 1999a), and sample transparency $\omega_T(\Delta 2\theta)$ (Ida and Kimura, 1999b). The function $f_S(\Delta 2\theta)$ is the convolution of the pseudo-Voigt function $f_{TCH}(\Delta 2\theta; W_G, W_L)$ determined by the full-width at half-maximum (FWHM) of the Gaussian and Lorentzian components, W_G and W_L (Thompson *et al.*, 1987), with the CuK α emission profile $f_\alpha(\Delta 2\theta)$ (Deutsch *et al.*, 2004). Two background parameters, intensity, peak position, and Gaussian

and Lorentzian width, $\{b_0, b_1, I, 2\theta_1, W_G, W_L\}$, are treated as adjustable parameters.

The results of the FPA fitting to LaB₆ 100-reflection are shown in Figures 2(a) and 2(b). The amount of errors estimated for the observed data and the errors caused by counting statistics are also shown in Figure 2(b). Most part of the errors estimated for the 100-peak is assigned to the propagation of 2θ -errors, and the results of fitting suggest overestimation of errors. It is not surprising, because the sensitivity of the strip detector should not be uniform, and the effective width of a strip detector is likely to be more restricted than the interval of the strips.

The optimized values of $K\alpha_1$ -peak location, marked by vertical arrows in Figures 2(a) and 2(c), are $2\theta_{100} = 21.3672$ (11) $^\circ$ and 21.36561 (12) $^\circ$ for the observed and deconvolved-convolved data, respectively. There is slight discrepancy between the above values of $2\theta_{100}$ beyond the estimated errors, but the apparent peak profile of the source data and the estimated peak positions in Figures 2(a) and 2(c) support that the deconvolution-convolution treatment automatically corrects the apparent peak shift caused by instrumental aberrations, similarly to the FPA-fitting method.

The optimized value of the FWHM of the Gaussian component of the FPA fit to the 100-reflection, $W_G = 0.003$ (12) $^\circ$, may appear to be consistent with that the deconvolved-convolved 100-reflection data also show Lorentzian-like profile with the optimized Pearson VII shape parameter of $\mu = 1.000$ (14), but the relation is not straightforward, because the deconvolved-convolved data are not intrinsic diffraction

peak profile, but the convolution with the symmetrized instrumental functions.

Figures 2(b) and 2(d) show a remarkable reduction of the estimated statistical errors through the deconvolution-convolution process. A tendency to underestimation of errors may be introduced by the neglect of the off-diagonal elements of the weight matrix on the deconvolution-convolution process, but the difference plot shown in Figure 2(d) still supports that the calculated errors are not heavily underestimated.

Figures 3 and 4 show the analytical results for 321 and 510-reflections. The FPA fitting for 510-reflection shows significant deviation from the observed data, but it should not be caused by possible faults of the assumed spectroscopic or instrumental parameters because the deconvolved-convolved data based on the same parameters do not show such significant deviation. The discrepancy in the results of FPA analysis is likely to be caused by the insufficient implementation of the model applied here.

D. Peak positions

The effects of automatic peak-shift correction expected to be achieved by both the FPA and deconvolution-convolution methods have been examined by evaluating the nominal lattice parameter a_{hkl} calculated from each peak position $2\theta_{hkl}$, by the following equation:

$$a_{hkl} = \frac{\lambda_{\alpha 1} \sqrt{h^2 + k^2 + l^2}}{2 \sin \theta_{hkl}}, \quad (29)$$

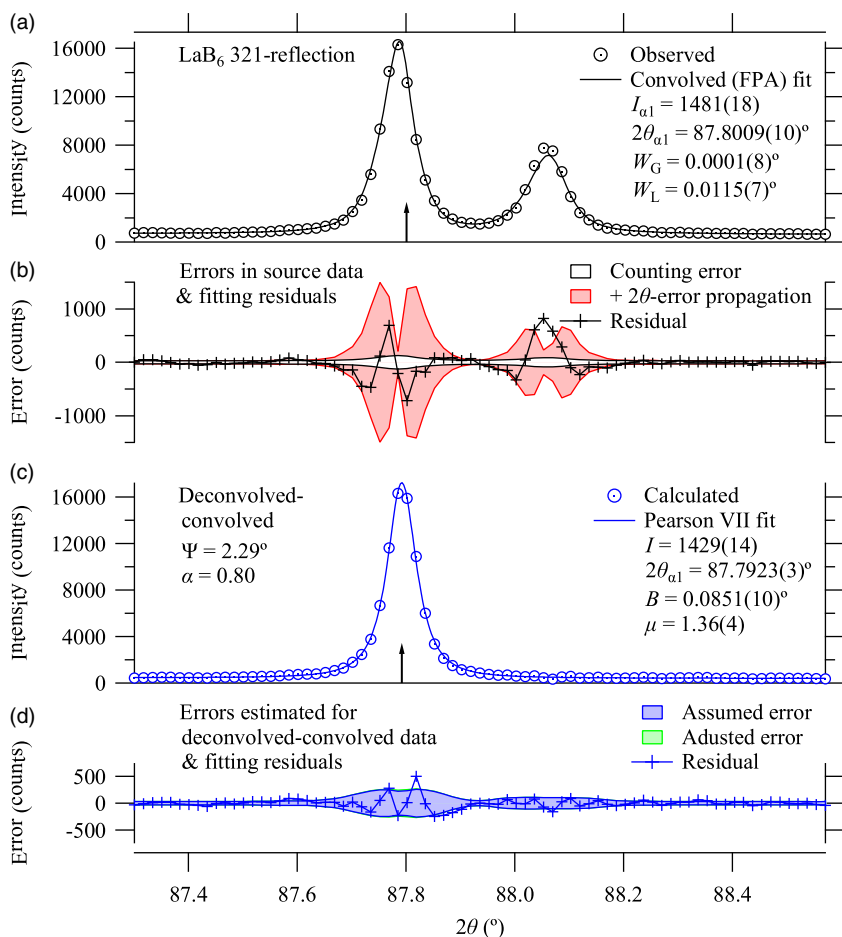


Figure 3. (Colour online) Observed data, fitting results to the observed data, deconvolved-convolved data, and fitting results to the deconvolved-convolved data about LaB₆ 321-reflection. See the caption of Figure 2 for the definitions.

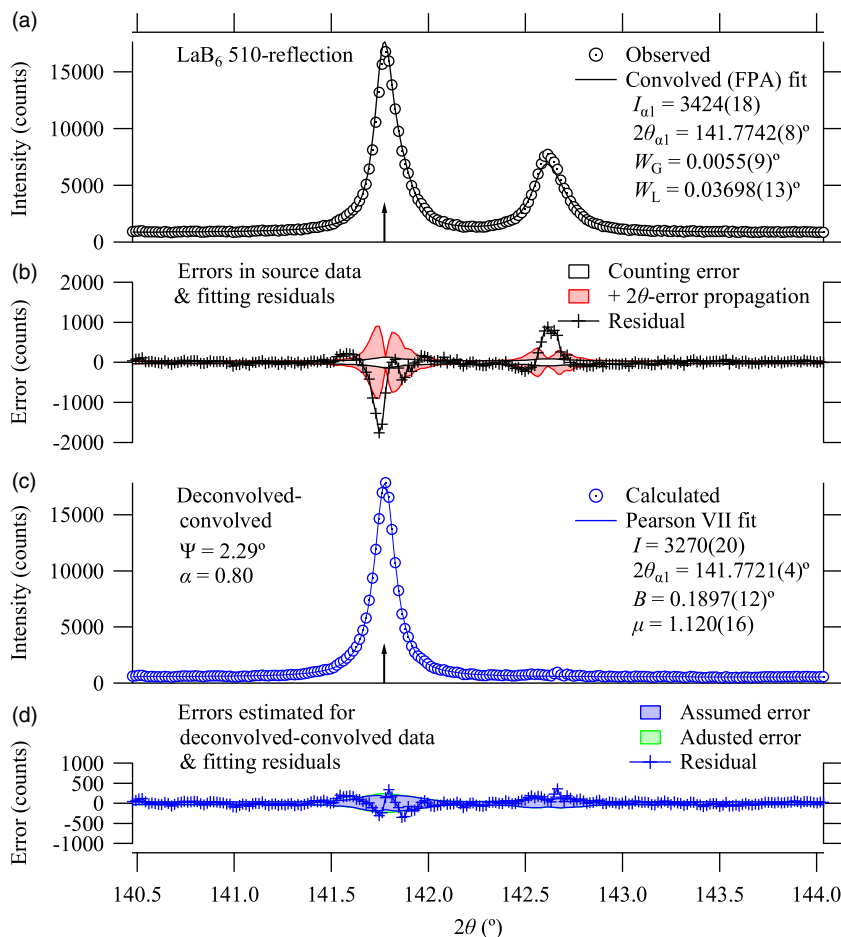


Figure 4. (Colour online) Observed data, fitting results to the observed data, deconvolved-convolved data, and fitting results to the deconvolved-convolved data about LaB₆ 510-reflection. See the caption of Figure 2 for the definitions.

where $\lambda_{\alpha 1} = 1.5405929 \text{ \AA}$ is the assumed CuK α_1 peak wavelength. The values of a_{hkl} calculated for 23 peak locations are plotted in Figure 5.

Firstly, a naive model for the peak shift (McCusker *et al.*, 1999) was applied, the formula of which to simulate the calculated lattice constant a_{hkl} is given by

$$a_{hkl} = \frac{a_{\text{true}} \sin \theta'_{hkl}}{\sin \theta_{hkl}}, \quad (30)$$

$$2\theta'_{hkl} = 2\theta_{hkl} - \Delta 2\Theta_0 + \frac{2\Delta S \cos \theta_{hkl}}{R}, \quad (31)$$

where a_{true} is the true lattice constant of LaB₆, $\Delta 2\Theta_0$ the constant error about the diffraction angle (zero offset), ΔS the displacement of the sample face from the rotation axis of the goniometer, and R is the goniometer radius. The errors in the calculated lattice constants, Δa_{hkl} , were estimated by the difference of the values calculated for $2\theta_{hkl}$ and $2\theta_{hkl} + \Delta 2\theta_{hkl}$, where $\Delta 2\theta_{hkl}$ is the error in $2\theta_{hkl}$ evaluated by the profile fitting as the propagation of the assumed errors in the intensity data.

The results for the values estimated by the FPA analysis are well reproduced by the naive model, and systematic deviation is not clear, as shown in Figures 5(a) and 5(b). It should be noted that no significant trend to suggest overestimation of errors in the estimated peak positions has been detected in Figure 5(b).

In contrast, the values estimated by the Pearson VII fitting to the deconvolved-convolved data are clearly deviated from the optimized naive model, as can be seen in Figure 5(c).

It is suggested that additional peak shift has artificially been introduced on the deconvolution-convolution treatment applying the approximate formula for the axial-divergence aberration. The naive model given by Eq. (31) is then replaced by a modified formula given by

$$2\theta'_{hkl} = 2\theta_{hkl} - \Delta 2\Theta_0 + \frac{2\Delta S \cos \theta_{hkl}}{R} - \Delta 2\Theta_1 (\tan \theta_{hkl} - \cot \theta_{hkl}), \quad (32)$$

where $\Delta 2\Theta_1$ is an additional adjustable parameter.

The modified model given by Eq. (32) certainly improves the fitting to the dependence of a_{hkl} on 2θ , as can be seen in Figure 5(c), and the additional parameter $\Delta 2\Theta_1$ has been optimized to be $0.00122(5)^\circ$. No systematic behavior of the residuals of the modified fitting is detected in the difference plot in Figure 5(d), and the values of residuals appear to be consistent with the estimated statistical errors.

Since the addition of the term in Eq. (32) is just a slight modification of the shift parameter used in the deconvolution-convolution calculation about the axial-divergence aberration, δ in Eq. (8), the adjustment of the shift can be easily implemented. The deconvolution-convolution treatment is then retried, just after replacing the shift parameter δ defined

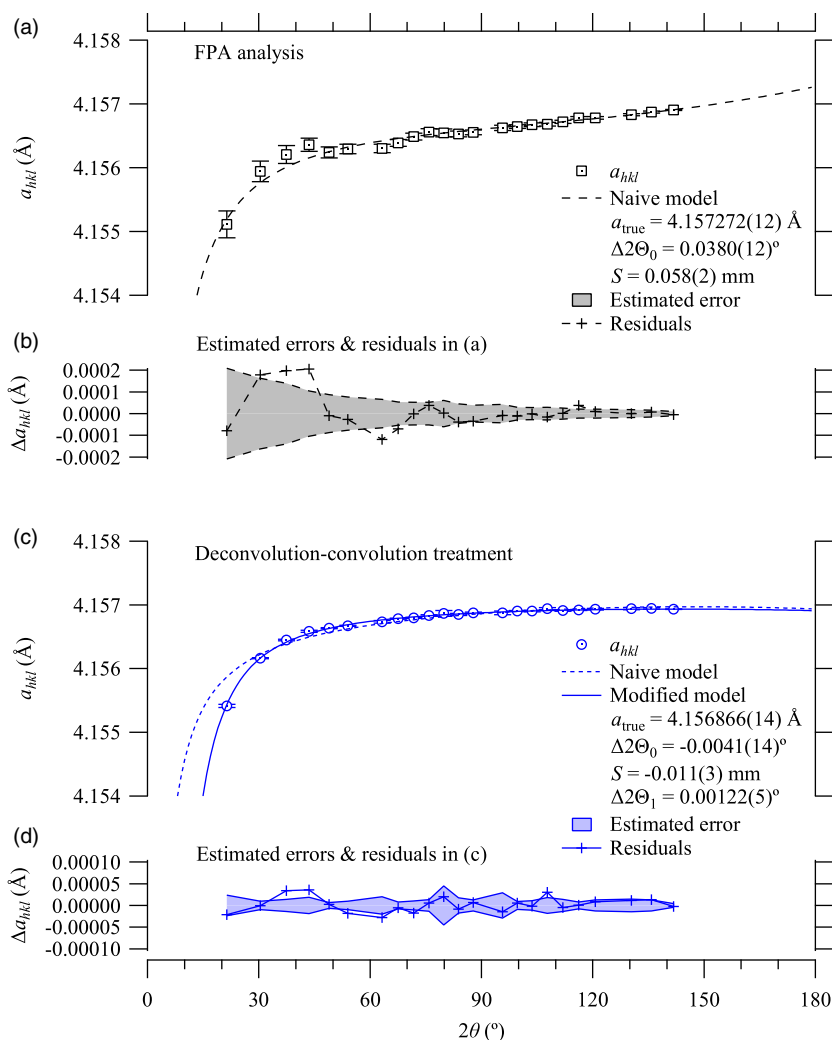


Figure 5. (Colour online) (a) Nominal lattice constants calculated from the 2θ peak positions evaluated by FPA analysis, and fitting curves calculated by a naive model, and (b) estimated errors and fitting residuals in (a), (c) Nominal lattice constants from deconvolution-convolution treatments, fitting curves calculated by naive and modified models, and (d) estimated errors and residuals of the modified fitting model.

in Eq. (9) by δ' , given by

$$\delta' = \delta - \frac{\Delta 2\Theta_1}{1 - \beta}. \quad (33)$$

The nominal lattice constants calculated from the data treated by the deconvolution-convolution method incorporating

the shift adjustment are shown in Figure 6. The apparent dependence on the diffraction angle is now reproduced by the naive model given by Eq. (31), as expected. The value of zero-offset error $\Delta 2\Theta_0$ estimated at $0.0006(4)^\circ$, and the sample displacement error ΔS estimated at $-0.0017(8)$ mm are both acceptable values. The value of lattice constant a_{true} is estimated at $4.156911(5)$ Å, while the certified value of

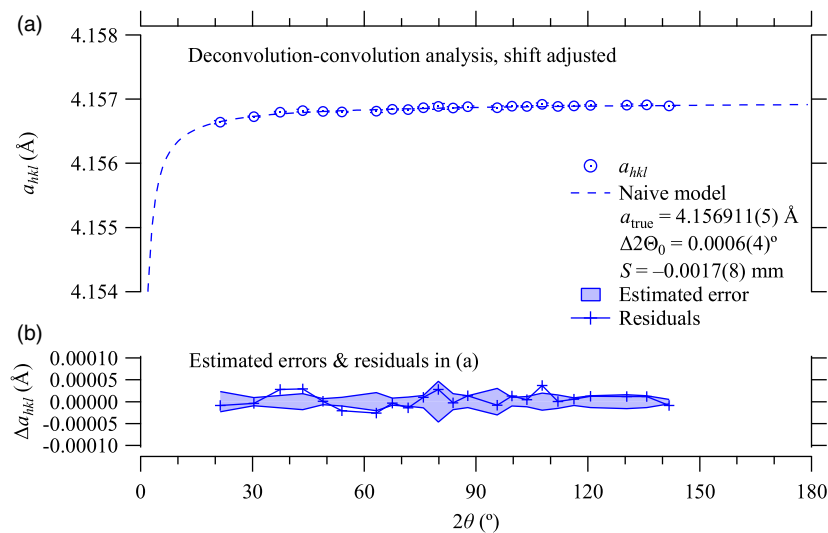


Figure 6. (Colour online) (a) Nominal lattice constants calculated after the shift adjustment on deconvolution-convolution process and fitting curve based on a naive model, and (b) estimated errors and fitting residuals.

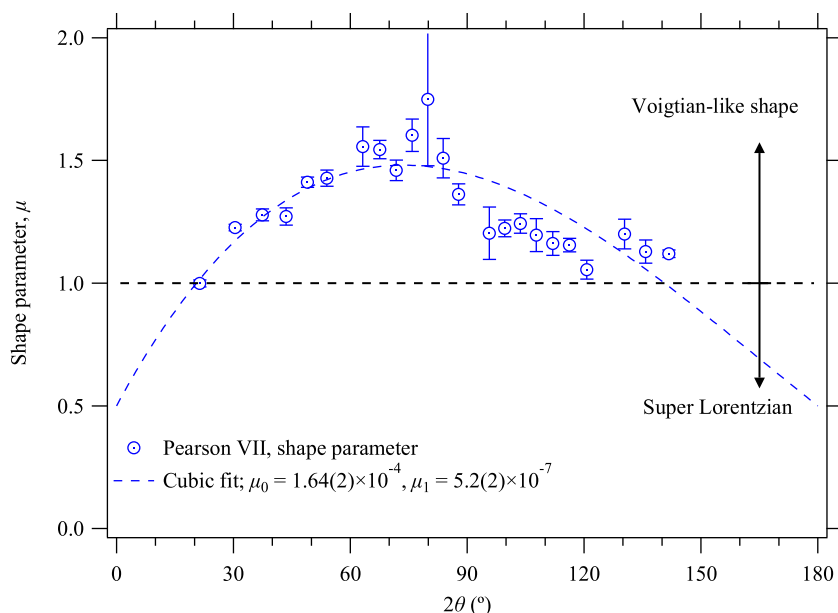


Figure 7. (Colour online) Pearson VII shape parameter μ optimized by individual profile fitting to the deconvolved–convolved data (circles), and a cubic fitting curve (broken line).

NIST SRM660a is $4.156916(10)$ Å at 22.5 °C. The true lattice constant a_{true} should be corresponded to the extrapolated value of a_{hkl} to the limit of $2\theta_{hkl} \rightarrow 180^\circ$ in the naive model for the peak shift, as can be seen in Figures 5 and 6, and it is generally difficult to certify the validity of extrapolation. Precise temperature control and repeated experiments with refilled powder sample should be required for more detailed discussions of accuracy or precision about the estimation of lattice constants. However, the results of FPA analysis shown in Figure 5(a) suggest that insufficient implementation of the FPA model might cause systematic deviation of the estimated peak positions and hence the systematic error on the evaluation of the lattice dimensions.

E. Peak shape

The optimized values of peak shape parameter μ of the Pearson VII peak profile function defined by Eq. (23) are plotted in Figure 7. The dependence of the shape parameter μ on 2θ shows maximum (minimum sharpness) at about $2\theta \approx 70^\circ$, and the sharpness of the peak shape increases on both sides of lower and higher diffraction angles. It should naturally be caused by increasing contribution of the effects of sharp axial-divergence aberration function for $2\theta \rightarrow 0^\circ$ and $2\theta \rightarrow 180^\circ$. Furthermore, the dependence also suggests that μ approaches $1/2$ at both the limits $2\theta \rightarrow 0^\circ$ and $2\theta \rightarrow 180^\circ$, where both the Pearson VII function and the axial-divergence aberration function would become singular. The asymmetry of the dependence on 2θ is also reasonable because the contribution of the spectral width of the source X-ray, modeled by a Lorentzian function similarly increases on the higher-angle side and the relative contribution of the axial-divergence function should be reduced as compared with that on the lower-angle side.

The dependence of μ on 2θ is then modeled by a cubic curve given by

$$\mu = \frac{1}{2} + (2\theta - 2\theta_0)(2\theta_1 - 2\theta)(\mu_0 + \mu_1 2\theta), \quad (34)$$

for the fixed values $(2\theta_0, 2\theta_1) = (0^\circ, 180^\circ)$. The adjustable

parameters (μ_0, μ_1) are optimized at $[1.64(2) \times 10^{-4}, 5.2(2) \times 10^{-7} (\text{°})^{-1}]$.

F. Integral breadth

The optimized values of the integral breadth B of the Pearson VII peak profile function defined by Eq. (23) are plotted in Figure 8. As the deconvolved–convolved peak profile is close to the Lorentzian profile, the integral breadth is modeled by

$$B = B_0 \tan \theta + B_1 + B_2 \cot \theta, \quad (35)$$

where B_0, B_1 , and B_2 are adjustable parameters. The optimized values are $B_0 = 0.0543(5)^\circ$, $B_1 = 0.02331(7)^\circ$, and $B_2 = 0.011113(2)^\circ$.

Since the $\text{CuK}\alpha_1$ FWHM is assumed to be 2.29 eV against the peak position 8047.83 eV (Ida *et al.*, 2018), the contribution of the spectral width to the coefficient B_0 is estimated at 0.051° as the integral breadth. As the interval of the Si detector strips and the effective width of the line-focus X-ray source are nominally 0.075 and 0.04 mm, the angular resolution for the goniometer radius of 240 mm is estimated at 0.0059° as the standard deviation, which can be related to the value estimated for the constant term B_1 in Eq. (35). The coefficients of $\tan \theta$ and $\cot \theta$ -terms of the broadening caused by axial-divergence aberration for $\Psi = 2.29^\circ$ should be corresponded to $\sqrt{17/1440}\Psi^2 = 0.010^\circ$ as the standard deviation, and the constant term in the axial-divergence aberration should be $\Psi^2/\sqrt{240} = 0.006^\circ$ as the standard deviation, as given in Eq. (3). The broadening caused by flat-specimen aberration should also be proportional to $\cot \theta$, but the effect is considered to be negligible in this case, because the coefficient is corresponded to $\Phi^2/\sqrt{45} = 0.0007^\circ$ as the standard deviation for the equatorial open angle of $\Phi = 0.5^\circ$.

G. Whole-pattern fitting

A whole-pattern fitting method known as the Pawley method (Pawley 1981) has been applied to the overall deconvolved–convolved data. Ninth-order polynomial of 2θ has

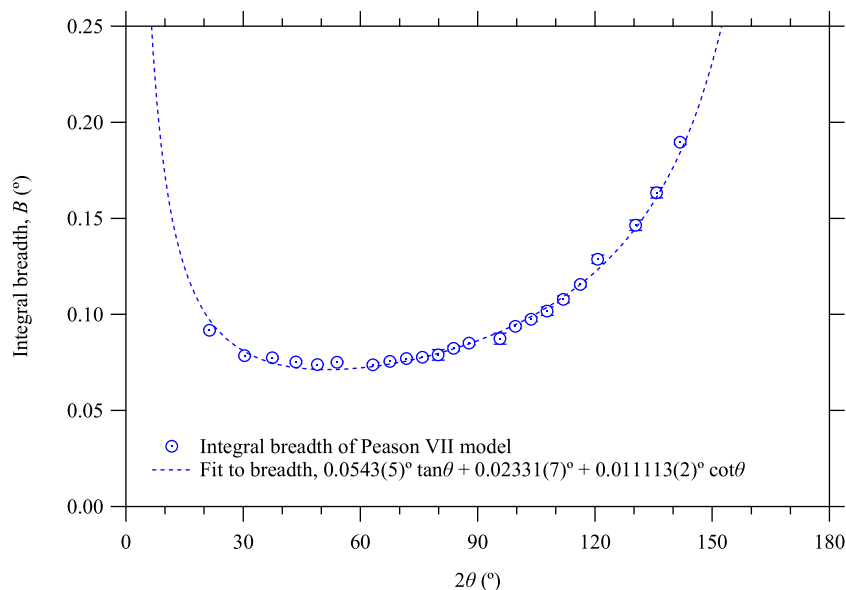


Figure 8. (Colour online) Integral breadth B optimized by individual profile fitting to the deconvolved–convolved data and a fitting curve.

been used for background intensity and the symmetric Pearson VII function is used as the peak profile function, the intensities of which are calculated in the range of ten times of integral breadth around the peak position. The overall intensities are modeled by the following equation:

$$y_j = \sum_{n=0}^9 b_n (2\theta_j)^n + \sum_{p=0}^{22} I_{p/P7} (2\theta_j - 2\theta_p; B(2\theta_p), \mu(2\theta_p)) \quad (36)$$

where the background parameters $\{b_n\}$, peak intensities $\{I_p\}$, lattice constant, zero-offset, and sample displacement, $\{a_{\text{true}},$

TABLE I. Integrated intensities of $\text{CuK}\alpha_1$ components evaluated by individual FPA profile fitting to source data (IPF-FPA/S), Pearson VII fitting to deconvolved–convolved data (IPF-P7/DC), and whole-pattern fitting to deconvolved–convolved data (WPF-P7/DC).

hkl	IPF-FPA/S	IPF-P7/DC	WPF-P7/DC
100	4600 (600)	5100 (40)	5009 (19)
110	8100 (500)	7890 (30)	7995 (19)
111	3240 (60)	3440 (20)	3396 (13)
200	1600 (40)	1782 (18)	1762 (10)
210	3600 (400)	4085 (18)	4125 (11)
211	2390 (80)	2249 (15)	2253 (9)
220	835 (16)	798 (10)	822 (8)
221/300	2180 (40)	2283 (14)	2355 (9)
310	1760 (20)	1615 (13)	1654 (9)
311	1077 (13)	1033 (10)	1077 (8)
222	185 (7)	174 (6)	179 (4)
320	720 (13)	671 (9)	692 (7)
321	1481 (18)	1429 (14)	1465 (12)
400	260 (7)	255 (8)	260 (5)
322/410	1360 (80)	1299 (13)	1317 (9)
330/411	1141 (19)	1093 (13)	1109 (9)
331	502 (10)	479 (10)	480 (7)
420	741 (10)	708 (11)	704 (8)
421	1590 (30)	1543 (15)	1539 (11)
332	860 (10)	834 (14)	800 (8)
422	607 (8)	584 (11)	596 (7)
500	757 (10)	734 (12)	737 (8)
431/510	3424 (18)	3270 (20)	3270 (16)

$\Delta 2\theta_0, \Delta S\}$ to determine the peak positions $2\theta_p$, and the width parameters $\{B_0, B_1, B_2\}$ defined in Eq. (35), and shape parameters $\{\mu_0, \mu_1\}$ in Eq. (34) are treated as adjustable parameters. The least-squares fitting assuming the propagation of the counting errors and 2θ -error propagation have been applied.

The values of optimized parameters are listed in Tables I and II. Figure 9 shows the result of whole pattern fitting. The R values are estimated at $R_p = 4.43\%$ and $R_{\text{wp}} = 5.32\%$, and the goodness-of-fit parameter at $S = 1.34$.

IV. CONCLUSION

An improved formula to simulate the effects of axial-divergence aberration in Bragg–Brentano geometry has been developed. Deformation of observed powder diffraction peak profile caused by axial-divergence aberration can effectively be removed by a deconvolution–convolution method based on the mathematical model. The powder diffraction peak profile of LaB_6 treated by the method has well been reproduced by a symmetric Pearson VII function. The peak positions of the deconvolved–convolved data can be simulated by a naive model about the possible zero-offset error and the displacement of the sample face. The overall peak profile in the deconvolved–convolved data have been modeled by three parameters to determine the integral breadth (width) and two parameters to determine the shape (sharpness), and

TABLE II. Lattice constant, peak shift, and profile parameters evaluated by individual FPA fitting to source data (IPF-FPA/S), individual Pearson VII fitting to deconvolved–convolved data (IPF-P7/DC), and whole-pattern fitting to deconvolved–convolved data (WPF-P7/DC).

Parameter	IPF-FPA/S	IPF-P7/DC	WPF-P7/DC
a (Å)	4.157272 (12)	4.156911 (5)	4.15687 (2)
$\Delta 2\theta_0$ (°)	0.0380 (12)	0.0006 (4)	0.0030 (10)
ΔS (mm)	0.058 (2)	−0.0017 (8)	0.018 (10)
B_0 (°)		0.0543 (5)	0.0519 (5)
B_1 (°)		0.02331 (7)	0.0288 (6)
B_2 (°)		0.011113 (2)	0.00977 (16)
μ_0		$1.64(2) \times 10^{-4}$	$1.59(2) \times 10^{-4}$
μ_1		$5.2(2) \times 10^{-7}$	$-4.8(2) \times 10^{-7}$

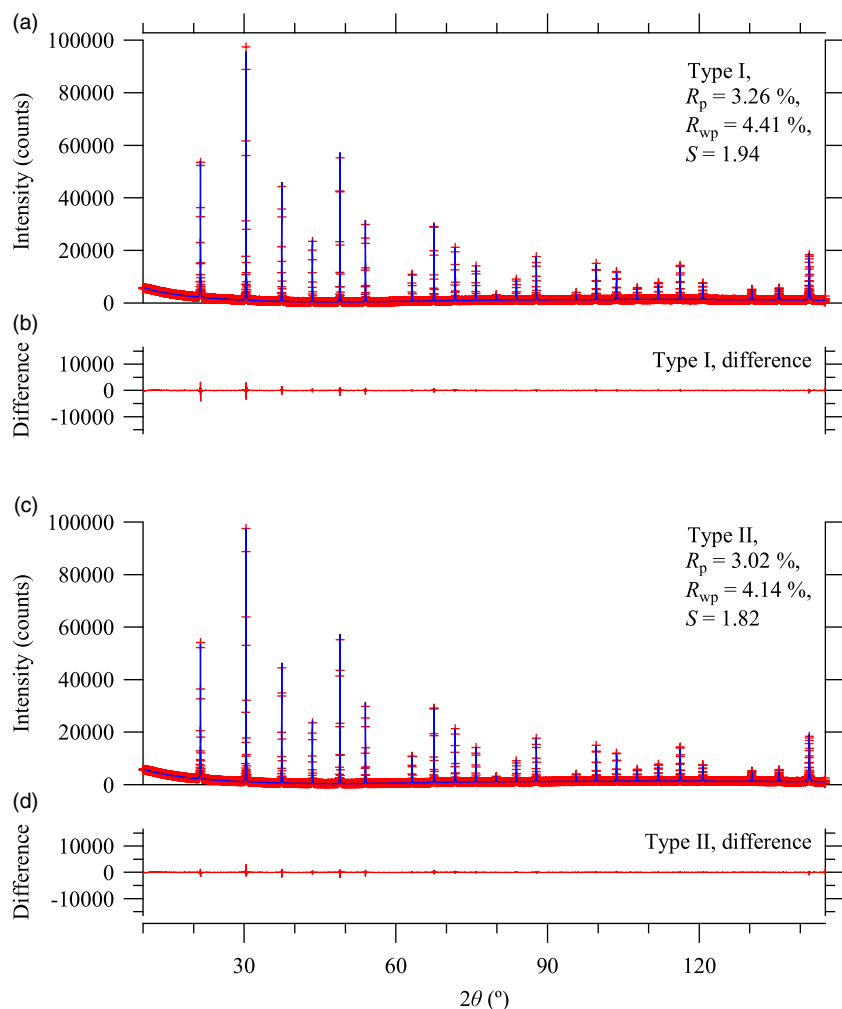


Figure 9. (Colour online) Results of whole pattern fitting to the deconvolved-convolved data.

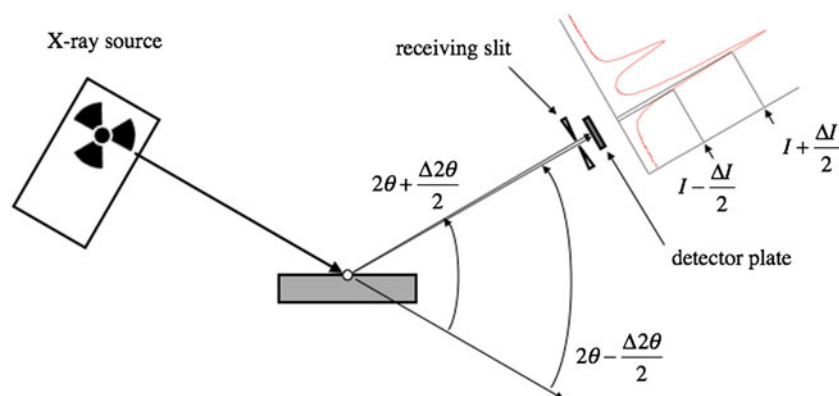


Figure 10. (Colour online) Schematic illustration to show the reason why the propagation of the error in the diffraction angle 2θ should be taken into account in the statistical analysis of the powder X-ray diffraction intensities.

the optimized values of the width-parameters are reasonably corresponded to the instrumental constants.

Antoniadis, A., Berruyer, J., and Filhol, A. (1990). "Maximum-likelihood methods in powder diffraction refinements," *Acta Crystallogr. Sect. A: Found. Crystallogr.* **46**, 692–711.

Cheary, R. W. and Coelho, A. (1992). "A fundamental parameters approach to x-ray line-profile fitting," *J. Appl. Crystallogr.* **25**, 109–121.

Deutsch, M., Förster, E., Hölzer, G., Hartwig, J., Hämmäläinen, K., Kao, C.-C., Huotari, S., and Diamant, R. (2004). "X-ray spectrometry of copper: new results on an old subject," *J. Res. Natl. Inst. Stand. Technol.* **109**, 75–98.

Ida, T. (1998). "Formula for the asymmetric diffraction peak profiles based on double Soller slit geometry," *Rev. Sci. Instrum.* **69**, 2268–2272.

Ida, T. (2008). "New measures of sharpness for symmetric powder diffraction peak profile," *J. Appl. Crystallogr.* **41**, 393–401.

Ida, T. (2016). "Experimental estimation of uncertainties in powder diffraction intensities with a two-dimensional X-ray detector," *Powder Diffr.* **31**, 216–222.

Ida, T. and Hibino, H. (2006). "Symmetrization of diffraction peak profiles measured with a high-resolution synchrotron X-ray powder diffractometer," *J. Appl. Crystallogr.* **39**, 90–100.

Ida, T. and Izumi, F. (2011). "Application of a theory for particle statistics to structure refinement from powder diffraction data," *J. Appl. Crystallogr.* **44**, 921–927.

Ida, T. and Izumi, F. (2013). "Analytical method for observed powder diffraction intensity data based on maximum likelihood estimation," *Powder Diffr.* **28**, 124–126.

- Ida, T. and Kimura, K. (1999a). "Flat-specimen effect as a convolution in powder diffractometry with Bragg-Brentano geometry," *J. Appl. Crystallogr.* **32**, 634-640.
- Ida, T. and Kimura, K. (1999b). "Effect of sample transparency in powder diffractometry with Bragg-Brentano geometry as a convolution," *J. Appl. Crystallogr.* **32**, 982-991.
- Ida, T. and Toraya, H. (2002). "Deconvolution of the instrumental functions in powder X-ray diffractometry," *J. Appl. Crystallogr.* **35**, 58-68.
- Ida, T., Goto, T., and Hibino, H. (2009). "Evaluation of particle statistics in powder diffractometry by a spinner-scan method," *J. Appl. Crystallogr.* **42**, 597-606.
- Ida, T., Ono, S., Hattari, D., Yoshida, T., Takatsu, Y., and Nomura, K. (2018). "Deconvolution-convolution treatment on powder diffraction data collected with Cu K α X-ray and Ni K β filter," *Powder Diffraction* **33**, 80-87.
- McCusker, L. B., Von Dreele, R. B., Cox, D. E., Lo \ddot{e} r, D., and Scardi, P. (1999). "Rietveld refinement guidelines," *J. Appl. Crystallogr.* **32**, 36-50.
- Pawley, G. S. (1981). "Unit-cell refinement from powder diffraction scans," *J. Appl. Crystallogr.* **14**, 357-361.
- Thompson, P., Cox, D. E., and Hastings, J. B. (1987). "Rietveld refinement of debye-scherrer synchrotron X-ray data from Al₂O₃," *J. Appl. Crystallogr.* **20**, 79-83.

Appendix A Calculation of cumulants of axial-divergence aberration function

The n th-order cumulant κ_n of a function $w(x)$ is generally defined by the following equation:

$$\kappa_n = \lim_{\theta \rightarrow 0} \left[\frac{\partial^n}{\partial \theta^n} \ln \int_{-\infty}^{\infty} e^{\theta x} w(x) dx \right]. \quad (\text{A1})$$

When $w(x)$ is a normalized function, the first-order cumulant:

$$\kappa_1 = \int_{-\infty}^{\infty} x w(x) dx \quad (\text{A2})$$

is identical to the average x , the second-order cumulant:

$$\kappa_2 = \langle x^2 \rangle - \langle x \rangle^2 \quad (\text{A3})$$

is identical to the variance $\langle (x - \langle x \rangle)^2 \rangle$, and the third-order cumulant:

$$\kappa_3 = \langle x^3 \rangle - 3\langle x^2 \rangle \langle x \rangle + 2\langle x \rangle^3 \quad (\text{A4})$$

is identical to the third-order central moment $\langle (x - \langle x \rangle)^3 \rangle$. Higher-order cumulants are also expressed by the combination of the average of n th power of x , $\langle x^n \rangle$.

When the instrumental function is expressed by the following formula:

$$w(x) = \int_{\alpha_{\min}}^{\alpha_{\max}} \delta(x - g(\alpha)) f(\alpha) d\alpha, \quad (\text{A5})$$

the average of n th power of x is calculated by

$$\langle x^n \rangle = \int_{-\infty}^{\infty} x^n w(x) dx = \int_{\alpha_{\min}}^{\alpha_{\max}} [g(\alpha)]^n f(\alpha) d\alpha. \quad (\text{A6})$$

Appendix B Derivation of scale transforms for axial-divergence aberration function

The basic idea of constructing the scale-transform formulas for a convolution model is not far from the one previously proposed (Ida and Toraya, 2002), where the scale transforms of $\chi'_+ = \ln \sin \theta$ for the upper component and $\chi'_- = -\ln \cos \theta$ for the lower component were applied. Since $\Delta 2\theta / \Delta \chi'_+ \propto \tan \theta$ and $\Delta 2\theta / \Delta \chi'_- \propto \cot \theta$, the first and third-order cumulants of the convolution $w(\chi'_+) * w(-\chi'_-)$ should be proportional to $(\tan \theta - \cot \theta)$ and $(\tan^3 \theta - \cot^3 \theta)$, respectively.

The formula in Eq. (5) is derived as a solution of the following relations:

$$\frac{\Delta 2\theta}{\Delta \chi'_+} \propto \tan \theta + \beta \cot \theta, \quad (\text{B1})$$

$$\frac{\Delta 2\theta}{\Delta \chi'_-} \propto \cot \theta + \beta \tan \theta. \quad (\text{B2})$$

Then the dependence of the third-order cumulant of the convolution model $[w(\chi'_+) * w(-\chi'_-)]$ on the diffraction angle 2θ should be given by $(\tan \theta + \beta \cot \theta)^3 - (\cot \theta + \beta \tan \theta)^3$. The dependence on 2θ becomes proportional to the third-order cumulant of the axial-divergence aberration function given in Eq. (4), when the following equation is satisfied:

$$\frac{3\beta}{1 + \beta + \beta^2} = \frac{81}{169}. \quad (\text{B3})$$

The value of β given in Eq. (6) is the solution of Eq. (B3). Even if the numerical value of the coefficient β estimated at 0.197562 is not large, it is expected that addition of this term improves the approximation than the previous formula (Ida and Toraya, 2002), as is supported by the coincidence of the third-order cumulant with the precise formula. The coincidence of the first-order cumulant (average) can be achieved by the constant shift of the component function, described in Appendix C.

Appendix C Adjustment of the formula of component functions

It is assumed that the component functions of a convolution model are given by

$$w_{\pm}(\chi_{\pm}) = \frac{1}{\gamma} g\left(\frac{\pm \chi_{\pm} - \delta}{\gamma}\right), \quad (\text{C1})$$

where $g(x)$ is a normalized function. When the first, second and third-order cumulants of the function $g(x)$ is given by $\langle x \rangle$, $\langle (\Delta x)^2 \rangle$ and $\langle (\Delta x)^3 \rangle$, respectively, the cumulants of the function $w_{\pm}(\chi_{\pm})$ are given by

$$\langle \chi_{\pm} \rangle = \pm \gamma \langle x \rangle + \delta, \quad (\text{C2})$$

$$\langle (\Delta \chi_{\pm})^2 \rangle = \gamma^2 \langle (\Delta x)^2 \rangle, \quad (\text{C3})$$

$$\langle (\Delta \chi_{\pm})^3 \rangle = \pm \gamma^3 \langle (\Delta x)^3 \rangle, \quad (\text{C4})$$

and the cumulants of the convolution of the component functions on the 2θ -scale should be given by

$$\langle 2\theta \rangle = \gamma \langle x + \delta \rangle (1 - \beta) (\tan \theta - \cot \theta), \quad (\text{C5})$$

$$\begin{aligned} \langle (\Delta 2\theta)^2 \rangle &= \gamma^2 \langle (\Delta x)^2 \rangle (1 + \beta^2) \\ &\times \left(\tan^2 \theta + \frac{4\beta}{1 + \beta^2} + \cot^2 \theta \right), \end{aligned} \quad (\text{C6})$$

$$\begin{aligned} \langle (\Delta 2\theta)^3 \rangle &= \gamma^3 \langle (\Delta x)^3 \rangle (1 - \beta^3) \\ &\times \left(\tan^3 \theta + \frac{3\beta \tan \theta}{1 + \beta + \beta^2} - \frac{3\beta \cot \theta}{1 + \beta + \beta^2} - \cot^3 \theta \right). \end{aligned} \quad (\text{C7})$$

The parameter γ is adjusted by the relation in Eq. (C7) for the given values of $\langle (\Delta 2\theta)^3 \rangle$, $\langle (\Delta x)^3 \rangle$ and β , and the parameter δ is then adjusted by the relation in Eq. (C5) for the given values of $2\theta_A$, x , β , and γ .

The first and third-order cumulants of the model function $w(x)$ applied here are given by $\langle x \rangle = \alpha\gamma + \delta$ and $\langle (\Delta x)^3 \rangle = 2\alpha\gamma^3$, and the value of γ given in Eq. (21) is the solution of the equation:

$$\frac{169\Psi^6}{60480} = 2\alpha\gamma^3 (1 - \beta^3), \quad (\text{C8})$$

and the value of δ in Eq. (20) has been determined by the equation:

$$\frac{\Psi^2}{12} = (\alpha\gamma + \delta)(1 - \beta), \quad (\text{C9})$$

Appendix D Invariance of even-order cumulants on the deconvolution–convolution process

Absolute values of cumulants of functions $f(x)$ and $f(-x)$ are equal, and the signal is unchanged for even-order and inverted for odd-order cumulants. The autocorrelation of the function $f(x)$, we here express by $|f|^2(x)$, is identical to the convolution of $f(x)$ and $f(-x)$. Since cumulants are additive on convolution, even-order cumulants of $|f|^2(x)$ become double of those of the function $f(x)$, and odd number cumulants of $|f|^2(x)$ are zero. When we define a function $|f|(x)$ by

$$|f|(x) \equiv \int_{-\infty}^{\infty} |F(k)| e^{-2\pi i k x} dk, \quad (\text{D1})$$

$$F(k) \equiv \int_{-\infty}^{\infty} f(x) e^{2\pi i k x} dx, \quad (\text{D2})$$

it is clear that the convolution of $|f|(x)$ with itself is identical to the autocorrelation $|f|^2(x)$. Then even-order cumulants of $|f|(x)$ are equal to those of $f(x)$, and odd-order cumulants of $|f|(x)$ are zero. We can confirm that the deconvolution with $f(x)$ and convolution with $|f|(x)$ only changes the odd-order

cumulants, but keeps even-order cumulants, including integrated intensity (zeroth-order cumulant), variance (second-order cumulant), kurtosis (excess or sharpness; fourth-order cumulant) unchanged.

Appendix E Bayesian interpretation of zero-count data

When we assume uniform prior probability distribution for the intensity y ,

$$P(y) = \begin{cases} 1/\varepsilon & [0 < y < \varepsilon] \\ 0 & [\text{elsewhere}] \end{cases}, \quad (\text{E1})$$

for an arbitrary large value of ε , and the likelihood function $P(n|y)$ of Poisson distribution for the observed count n ,

$$P(n|y) = \frac{y^n e^{-y}}{n!}, \quad (\text{E2})$$

the probability for n counts $P(n)$ is given by

$$\begin{aligned} P(n) &= \int_{-\infty}^{\infty} P(n|y)P(y)dy \\ &= \frac{1}{\varepsilon} \lim_{\varepsilon \rightarrow \infty} \int_0^{\varepsilon} \frac{y^n e^{-y}}{n!} dy = \frac{1}{\varepsilon}. \end{aligned} \quad (\text{E3})$$

Bayesian inference derives the posterior probability distribution from the observed count n given by

$$P(y|n) = \frac{P(n|y)P(y)}{P(n)} = \frac{y^n e^{-y}}{n!}. \quad (\text{E4})$$

The posterior probability for zero count is given by $P(y|0) = e^{-y}$, and the expected values of average and variance are then both unity.

Appendix F Propagation of error in 2θ

It seems that most of the analyses about powder X-ray diffraction data are based on the assumption that the observed diffraction intensity I can be connected with a certain value of the theoretical diffraction angle 2θ . However, the size of the detector element is finite, no matter which type of a detector, a zero-dimensional, one-dimensional, or two-dimensional detector is used.

Figure 10 illustrates why it is considered to be necessary to take into account the errors in the goniometer angle 2θ , the latter of which may be provided from a data acquisition system to users, to achieve statistical analysis of the observed diffraction intensity data.

If the center of a detector element of $\Delta 2\theta$ in width is located at the position of 2θ , it will detect the X-ray photons diffracted at the angles ranging from $2\theta - \Delta 2\theta/2$ to $2\theta + \Delta 2\theta/2$. It is expected that the detected intensities range from $I - \Delta I/2$ to $I + \Delta I/2$.